
Research article

A two- to three-dimensional wake transition mechanism induced by the angle of attack of a NACA0012 airfoil

Hussein Kokash and G. Gilou Agbaglah*

Department of Mechanical Engineering, Wayne State University, Detroit, MI 48202, USA

* **Correspondence:** Email: gilou.agbaglah@wayne.edu; Tel: +1-313-577-5148; Fax: +1-313-577-8789.

Abstract: A high-order spectral element method was used to perform three-dimensional direct numerical simulations of the flow past a NACA0012 airfoil. We considered a Reynolds number $Re = 1000$ and two different angles of attack, $\alpha = 11^\circ$ and $\alpha = 16^\circ$, to study the two- to three-dimensional wake transition. A boundary layer separation was observed for both angles of attack with the separation point closer to the leading edge for $\alpha = 16^\circ$. The downstream of the airfoil exhibited streamwise vortical structures formed in the braid regions connecting the primary vortices for $\alpha = 16^\circ$, while only shed vortices were observed for $\alpha = 11^\circ$. The formation of these streamwise structures were explained by the presence of a reverse flow from the lower surface for $\alpha = 16^\circ$, enhancing shearing effects. The early-stage development of the three-dimensional wake, in the case of $\alpha = 16^\circ$, was characterized by the formation of a spanwise sinusoidal velocity whose amplitude increased exponentially over time. The flow on the upper surface experienced a higher strain field which pulled up small disturbances from the airfoil surface and formed regions of concentrated vortical structures. These structures were subjected to stretching under the strain field and later advected downstream of the airfoil.

Keywords: NACA0012 airfoil; direct numerical simulation; flow instability; three-dimensional transition; vortex dynamics

1. Introduction

In recent years, there has been a rapid development of aircraft designed for low-speed operations. These aircraft include high-altitude, long-endurance unmanned air vehicles (UAVs), as well as high-performance micro-air vehicles (MAVs). A key challenge in designing such aircraft is to understand and quantify the impact of low Reynolds numbers [$O(10^4)$] on their performance [1, 2]. The aerodynamics of airfoils operating at low Reynolds numbers is significantly affected by the potential deterioration of the lift-to-drag ratio [3, 4], flow separation [5, 6], unsteady flow parameters [7], as well as the presence of nonlinear and turbulent flows [8, 9]. At these Reynolds numbers, the flow over the airfoil and the

wake present complexity during the transition to turbulence through markedly distinct flow patterns in response to changes introduced in the flow parameters, such as the Reynolds number, $Re = U_\infty c / \nu$, where U_∞ represents the free-stream velocity, c the chord length of the airfoil, and ν the kinematic viscosity; or the geometric parameters, including the airfoil's relative thickness and angle of attack α [10, 11].

The flow over airfoil geometries experiences separation on the airfoil's upper surface due to the adverse pressure gradient. The nature of the separation is affected by both flow conditions and geometrical parameters. Especially, the location of the flow separation along the wing's chord is affected. The transitional flow region typically forms near the wing's trailing edge at lower angles of attack and shifts toward the leading edge as the angle increases [12, 6]. This shift significantly impacts the flow behavior, for instance the characteristic frequency of vortex shedding of the separated flow and the interactions with the wake [13]. In addition, a longer separation region is observed, until a point where the flow fails to reattach, contributing to a destabilization of the boundary layer and a transition to turbulence at the leading edge with a potential significant decrease in lift [14, 15], also known as a stall. Existing research on the aerodynamics of airfoils associates the laminar-to-turbulent transition to the flow disturbances within the separation bubble, where a Kelvin-Helmholtz-type instability is observed to lead the formation of vortices in the shear layer [13]. Additionally, the presence of spanwise coherent vortical structures can be a contributing factor in the laminar-to-turbulent transition process [16, 17].

The unsteady flow dynamics around the NACA0012 airfoil (a zero camber around the suction (top) and pressure (bottom) surfaces of the airfoil, with a maximum thickness of 12% of the chord length c) and its wake flow transitions at low Reynolds numbers are the subject of various investigations in recent years, both experimentally [18, 19] and numerically [20, 10]. For instance, it is found that the turbulent intensity has a more pronounced effect at lower Reynolds numbers ($10^3 < Re < 10^5$) than at higher Re on the shear layer separation and reattachment, the transition and the formation of the separation bubble [19]. [20] analyzed the transition to turbulence using numerical simulations for Reynolds numbers 10^2 – 10^4 and identified two main mechanisms: the aperiodicity beyond the von Kármán and the development of a shear-layer instability, due to the oscillation of the separation point downstream of the leading edge. In the study of [21], where particle image velocimetry (PIV) was used, five specific flow patterns around the NACA0012 airfoil were identified, for a range of angles of attack at Reynolds numbers smaller than 2500. These patterns include the steady attached flow, the formation of trailing and separation vortices, the emergence of a leading-edge vortex, and the bluff-body effect.

A comprehensive understanding of the transition to turbulence requires careful consideration of the transient flow. As such, a comprehensive exploration of the aerodynamic characteristics and flow structures in the transient stage holds significant engineering and academic importance [22], specifically, the two- to three-dimensional wake transition, which precedes the transition to a fully turbulent flow regime. This transition refers to the bifurcation in wake flow from a 2D state, characterized by the periodic von Kármán vortex shedding, to a 3D flow characterized by the formation of streamwise vortices. The three-dimensionality of the wake is shown to impact the characteristics of the flow, where the two-dimensional vortex shedding becomes absolutely unstable to three-dimensional perturbations [17]. The instability patterns observed in airfoil wakes closely resemble those identified in the wake of bluff bodies, i.e., cylinders [17]. Wavelengths of the associated three-dimensional structures are compared using a characteristic length $d = c \sin(\alpha)$ for the airfoil case [23]. In the case of cylinders with square or circular cross-sections, distinct secondary instability modes, referred to as Mode *A* and Mode *B*, are observed at specific Reynolds numbers. Williamson [24, 25] experimentally identified

these modes during the wake transition of a circular cylinder, with Mode *A* emerging at approximately $Re \approx 190$ and Mode *B* at higher Reynolds numbers. Barkley and Henderson [26] confirmed these findings through three-dimensional Floquet stability analysis, accurately predicting the critical Reynolds numbers and spanwise wavelengths for both modes. For square cylinders, Robichaux et al. [27] conducted similar analyses and identified comparable three-dimensional instability modes. Saha et al. [28] and Luo et al. [29] observed these modes in numerical simulations, noting that the wake structures closely resemble the vortex dynamics seen in circular cylinders. These modes are characterized by the differences in their spanwise wavelength and vortical structures. As the Reynolds number increases, the first three-dimensional unstable mode, Mode *A*, is identified by a long wavelength and tongue-like streamwise vortical structures [25, 28, 29]. Subsequently, Mode *B* emerges at higher Reynolds numbers, distinguished by the rib-like streamwise vortical structures and a shorter wavelength [25, 30, 29]. An interaction mode, Mode *A* – *B*, in which Mode *A* has a destabilizing effect on Mode *B* and Mode *B* has a stabilizing effect on Mode *A* with a resulting mixed-mode state over a range of Reynolds numbers is also observed [31]. A third mode, the sub-harmonic mode *C*, is observed and exhibits a wavelength between that of Modes *A* and *B* [26, 27, 32].

In the context of airfoils, the literature reports a limited number of studies investigating the influence of different flow parameters on the appearance of three-dimensionality in the wake. In the case of the NACA0012 airfoil, it is shown that a three-dimensional transition occurs in the wake for $400 \leq Re \leq 1000$ for a fixed angle of attack, $\alpha = 20^\circ$, through the sub-harmonic instability Mode *C* [33]. [34] studied the wake of an NACA0015 airfoil for Reynolds numbers smaller than 1800. They reported that at $\alpha < 15^\circ$, Mode *C* is observed while for $\alpha \geq 15^\circ$, Mode *A* and a quasi-periodic instability, Mode *QP* appear. [35] investigated the wake of three different NACA airfoils, namely the NACA0009, NACA0015, and NACA4415, at $Re < 600$ and reported different transition Reynolds numbers depending on the geometry of the airfoil. [36] studied the wake transitions of an NACA0012 airfoil for angles of attack in the range of $0^\circ \leq \alpha \leq 20^\circ$ and Reynolds numbers $500 \leq Re \leq 5000$. Their results show that Mode *C* is the first three-dimensional unstable mode to appear over the Reynolds number range studied. The transition to three-dimensionality of the airfoil wake is also demonstrated to occur at a constant Re as the angle of attack α increases. For instance, the flow transitions to three-dimensionality at $Re = 1000$ as the angle of attack increases from $\alpha = 13^\circ$ [36, 37]. A transition map is presented in [36], where it is determined that the critical angle of attack for the onset of three-dimensional flow scales as $\alpha_{3D} \sim Re^{-0.5}$.

Although considerable research has been conducted on the aerodynamics of airfoils at low Reynolds numbers, our understanding of wake transitions is far from sufficient [38]. Most studies, including those cited above, have focused more on characterizing different wake patterns and instability modes than on the physical mechanisms leading to their occurrence, which remain poorly understood. In this work, we use three-dimensional numerical simulations of the flow past the NACA0012 airfoil to investigate the three-dimensionality of the wake when increasing the angle of attack. We focus on the early stages of the three-dimensional flow development. Specifically, we compare the initial transient flows at two angles of attack: $\alpha = 11^\circ$ and 16° , which have previously been identified as exhibiting two-dimensional and three-dimensional wakes at $Re = 1000$, respectively [36, 37].

2. Numerical methods and simulations

A sketch illustrating the configuration of the computational domain and the coordinate system is shown in Figure 1(a). The airflow over the airfoil moves from the entrance on the left to the exit on the right, with the origin of the Cartesian coordinates positioned at the airfoil's leading edge when the airfoil is fully deployed and aligned with the flow direction ($\alpha = 0^\circ$).

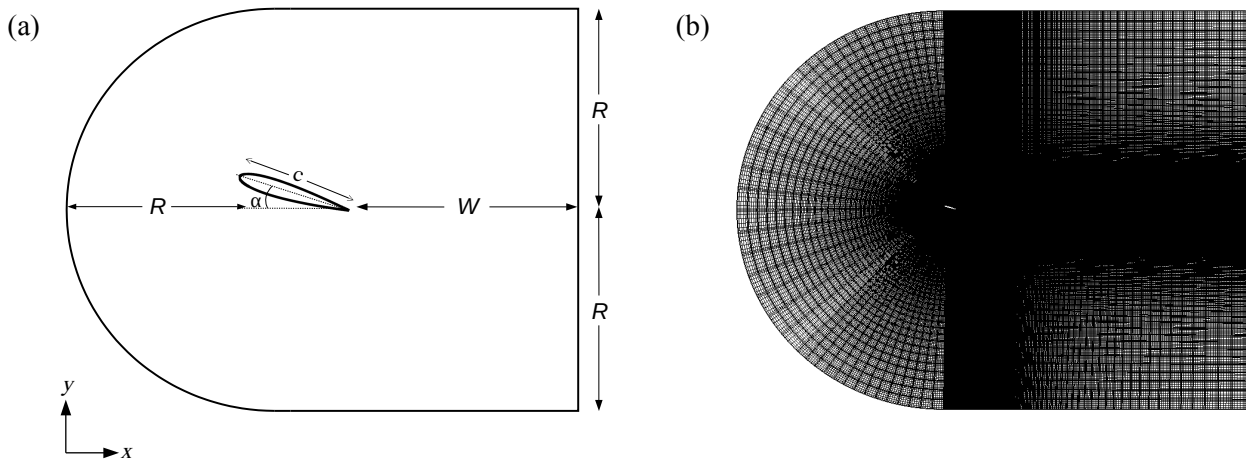


Figure 1. (a) Schematic of the computational domain and the airfoil, showing the chord length c , angle of attack α , domain radius R , and wake length W . Note that the domain schematic is not to scale. (b) Two-dimensional cross-section illustrating the mesh distribution of the computational domain around the NACA0012 airfoil.

The motion of the flow is governed by the incompressible Navier-Stokes equations, where the density ρ and viscosity μ are constants:

$$\nabla \cdot \mathbf{u} = 0 \quad (2.1a)$$

$$\rho \left(\frac{\partial \mathbf{u}}{\partial t} + \mathbf{u} \cdot \nabla \mathbf{u} \right) = -\nabla p + \mu \nabla^2 \mathbf{u} \quad (2.1b)$$

Here, \mathbf{u} represents the velocity vector and p the pressure.

The Navier-Stokes equations (2.1a) and (2.1b) are solved using the high-order spectral element method [39], developed in Nek5000 [40]. The governing equations are discretized using the Galerkin method. In this approach, the computational domain is divided into K hexahedral spectral elements, upon which the solution is approximated by tensor products of N th-order Legendre polynomial Lagrangian interpolants. The time derivative is discretized via a second-order implicit backward differentiation and nonlinear convective terms are advanced using an explicit fourth-order Runge–Kutta scheme. Further details can be found elsewhere, e.g., [41]. Figure 1(b) provides a side view of the domain's grid distribution.

The dimensions of the computational domain can have a significant impact on simulation results. Therefore, it is essential to use a domain size that reduces boundary effects while retaining the constraints of available computing resources. In this work, we adopt a C-grid computational domain topology, with a radius R and a wake length W , as illustrated in Figure 1(a). The use of a C-grid topology allows the curvature of the computational grid to match the airfoil's leading edge curvature [42]. In the present

simulations, the airfoil's chord length c corresponds to 1m and the computational domain extends 13 and 19 chords for the domain radius R and wake length W , respectively. The selected domain size effectively mitigates the occurrence of unwanted reflections originating from the outflow boundaries [43, 17, 5]. A spanwise length of 6 chords is used. It is noteworthy that no significant effect of the domain span length is observed on the flow characteristics [44]. The selection of a domain span length of $6c$ is deemed effective for capturing the long wavelengths that may arise in the wake. A constant inflow velocity, U_∞ , is imposed at the inlet boundary, while an outflow boundary condition is applied at the exit. Neumann-type boundary conditions are employed at the upper and lower boundaries of the domain (i.e., the "SYM" boundary condition in Nek5000). These conditions impose a zero y -derivative and a zero value for the normal velocity at the boundaries which is equivalent to a free-slip impermeable boundary. Periodic boundary conditions are imposed at the domain's spanwise boundaries and a no-slip condition is imposed at the airfoil boundaries.

The considered mesh closely follows that used in [43], where mesh convergence is achieved. The 3D mesh is generated by simply extruding the structured 2D mesh in the spanwise direction. The 2D mesh consists of a total of $K = 25,752$ elements in the x - y plane and the spanwise direction is resolved using 6 equally sized elements. A polynomial order $N = 7$ is used, with a total of 130,560 spectral elements in 3D. This configuration corresponds to approximately 44 million grid points within the computational domain, and a minimum mesh spacing of $2 \times 10^{-3}c$. The element density is high near the surface of the airfoil to accurately resolve the boundary layer, decreasing progressively toward the far field. A time step size of $\Delta t = 1.52 \times 10^{-4}$ is used.

In this work, a fixed Reynolds number, $Re = 1000$, is chosen, in line with prior experimental and numerical studies [10, 37, 45]. Two different angles of attack, $\alpha = 11^\circ$ and $\alpha = 16^\circ$, previously shown to trigger the three-dimensionality of the wake [37], are considered and make it possible to compare the two-dimensional wake at $\alpha = 11^\circ$ to the development of the three-dimensional flow obtained at $\alpha = 16^\circ$. The spanwise flow development and the analysis of vortical interactions on the airfoil's suction (top) surface are described below.

3. Wake dynamics

Three-dimensional simulations of the airflow dynamics around the NACA0012 airfoil are performed at $Re = 1000$ with $\alpha = 11^\circ$ and 16° . The computations for both angles of attack are performed over approximately 10 days using 100 CPUs, corresponding to 2.4×10^4 CPU hours. Table 1 presents integral flow characteristics, namely the time-averaged drag coefficient ($\overline{C_D}$), lift coefficient ($\overline{C_L}$), and Strouhal number (St) for angles of attack $\alpha = 11^\circ$ and $\alpha = 16^\circ$ for $Re = 1000$. The obtained values are found to be consistent with those reported by Kouser et al. [37]. In their work, a $\overline{C_D}$ value of 0.165 and $\overline{C_L}$ of 0.415 at $\alpha = 10^\circ$, and a $\overline{C_D}$ of 0.265 and $\overline{C_L}$ of 0.634 at $\alpha = 15^\circ$, were reported for $Re = 1000$.

Table 1. Time-averaged drag coefficient ($\overline{C_D}$), lift coefficient ($\overline{C_L}$), and Strouhal number (St) at different angles of attack for $Re = 1000$.

α	$\overline{C_D}$	$\overline{C_L}$	St
$\alpha = 11^\circ$	0.179	0.420	0.8667
$\alpha = 16^\circ$	0.214	0.629	0.6769

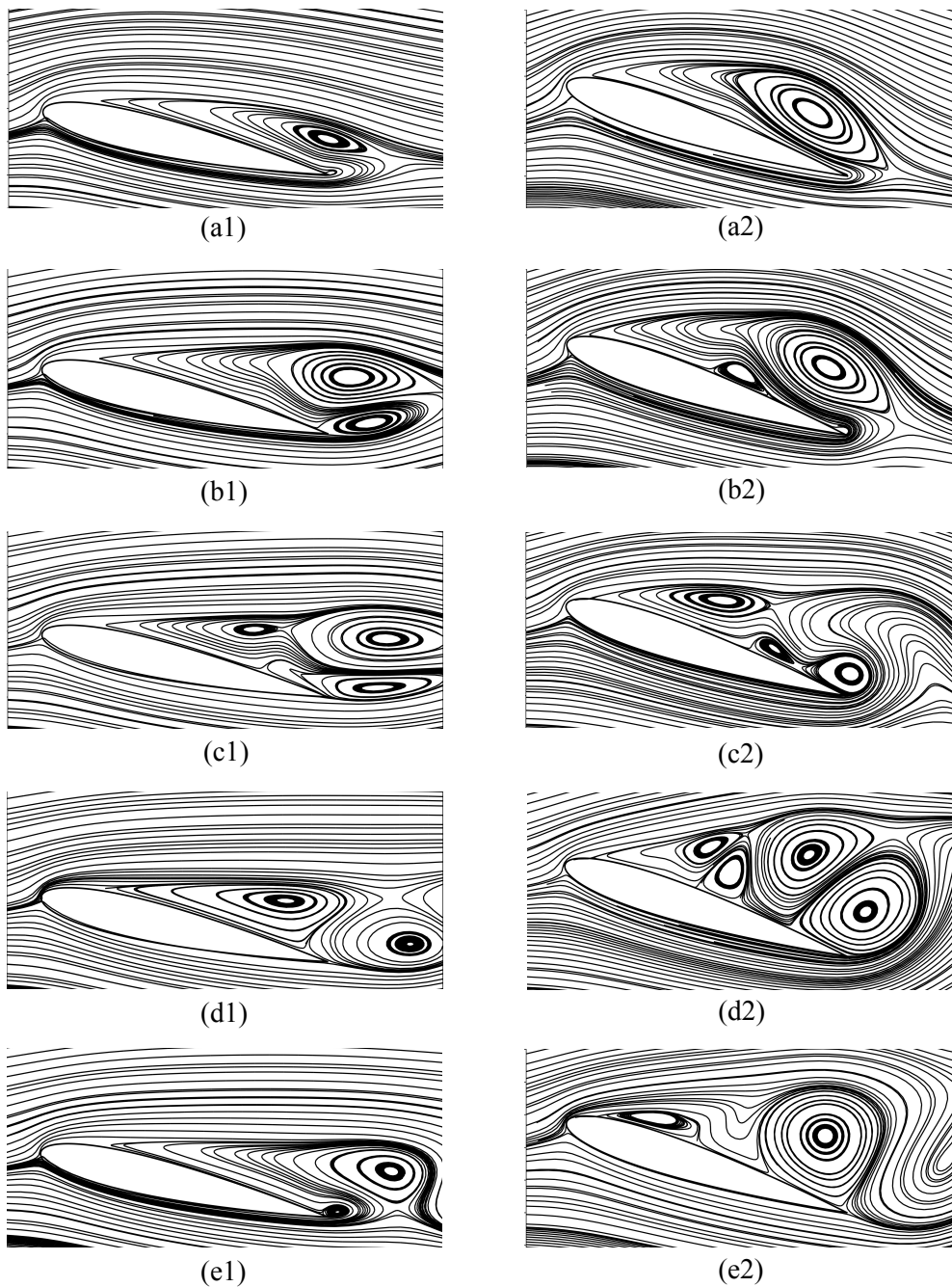


Figure 2. Time sequence of the streamlines around the airfoil surface showing the formation and interaction of spanwise vortices for $\alpha = 11^\circ$ (a1–e1), and $\alpha = 16^\circ$ (a2–e2). The time is increasing from top to bottom with $tU_\infty/c = 3.2, 4.9, 6, 7.9, 8.6$ for (a1–e1) and $tU_\infty/c = 3, 3.4, 4, 4.6, 5.3$ for (a2–e2).

In both cases, a boundary layer separation, accompanied by the formation of a separation bubble, is first observed at the suction (top) side near the leading edge once the flow passes the airfoil. This is known as the result of an adverse pressure gradient which occurs at the surface as the airflow decelerates. Next, the well-known von Kármán vortex street, consisting of a repeating vortex shedding from the top and bottom shear layers, is observed downstream of the airfoil. The repeating shedding cycle of the swirling vortices is markedly different for the two angles of attack, as shown in Figure 2. For $\alpha = 11^\circ$, the leading-edge vortex is advected downward at the trailing edge and interacts with the roll-up formed by the separated shear layer of the bottom surface. Both roll-up vortices are next shed downstream and the cycle starts again. In the case of $\alpha = 16^\circ$, the shedding cycle is different mainly due to the reverse flow formed on the top surface by the flow from the bottom side of the airfoil. In fact, the shear layer of the bottom surface separates at the trailing edge and turns around to climb onto the upper surface, allowing the interaction of counter-rotating vortices on the upper surface of the airfoil before they are shed downstream. The formation of these counter-rotating vortices on the surface of the airfoil is at the origin of the subsequent instability in the spanwise direction as will be shown later.

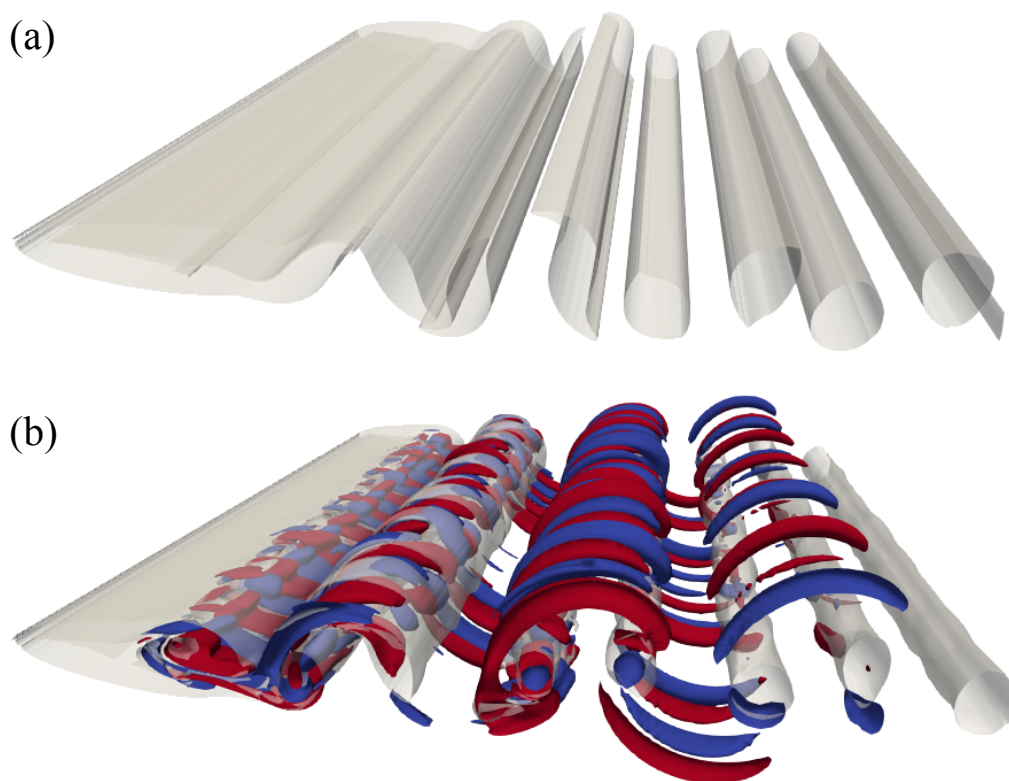


Figure 3. Iso-contours of streamwise vortices in the wake of the NACA0012 airfoil at $tU_\infty/c = 40$ for $\alpha = 11^\circ$ (a) and $\alpha = 16^\circ$ (b). Positive (red color) and negative (blue color) streamwise vortices are shown for $\alpha = 16^\circ$ and absent for $\alpha = 11^\circ$. Contours of the velocity magnitude are also displayed in gray colors.

As expected, a transition to three-dimensional flow is observed in the wake for $\alpha = 16^\circ$. Three-dimensional streamwise vortical structures are formed in the braid regions (regions between primary von Kármán vortices). However, only straight vortex tubes are displayed in the wake for $\alpha = 11^\circ$, as

depicted in Figure 3. The wake, at $\alpha = 11^\circ$ in Figure 3(a), is marked by the absence of the streamwise structures, see Figure 3(b). The alternating pattern formed by the positive and negative streamwise vorticity in Figure 3(b) closely resembles the rib-like vortex structures observed in the wake of a cylinder [46, 27, 47, 48, 49]. The three-dimensional instability at $\alpha = 16^\circ$ with the formation of streamwise structures suggests a pitchfork bifurcation, akin to observations in flow past cylinders [31, 32].

We next focus on the spanwise flow development by analyzing the time evolution of the spanwise component of the velocity field, w , downstream of the airfoil. Since the inlet velocity is two-dimensional, as specified by the boundary conditions, the wake flow becomes three-dimensional when w is considerably nonzero. The inflow velocity is initially two-dimensional, with a uniform streamwise component and no velocity in the normal or spanwise directions. As the flow evolves, the wake becomes three-dimensional when the spanwise velocity component w becomes significantly nonzero. In order to trace this transition, w is recorded downstream of the trailing edge on a line in the z -direction, passing through the point $(x = 1.5c, y = 0)$ of the x - y plane, for both $\alpha = 11^\circ$ and $\alpha = 16^\circ$. A nonzero spanwise velocity, exhibiting a sinusoidal shape with increasing amplitude, is obtained for $\alpha = 16^\circ$, while it remains approximately zero with no amplification for $\alpha = 11^\circ$ as shown in Figure 5.

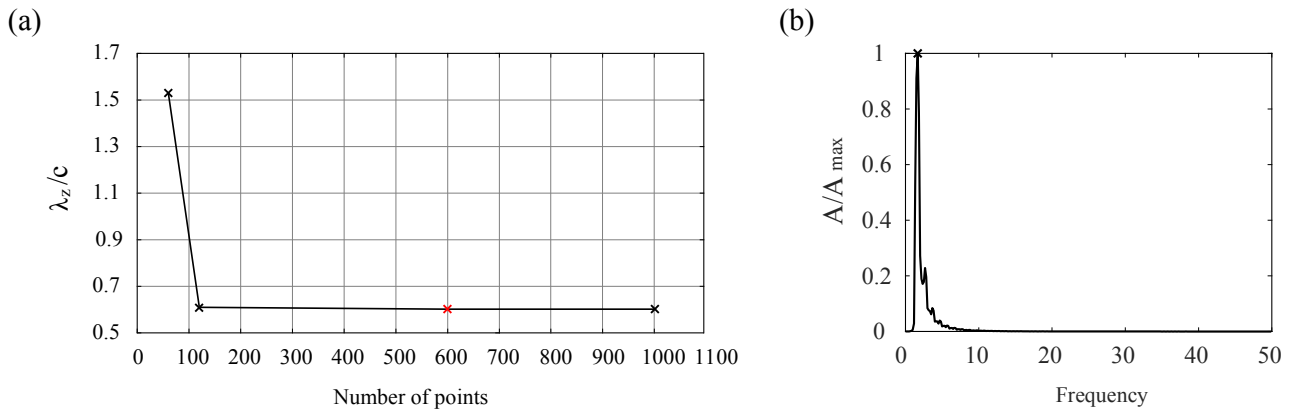


Figure 4. (a) Convergence of the wavelength calculation using a different number of points in the z -direction. (b) A fast Fourier transform (FFT) of the spanwise velocity at $tU_\infty/c = 20$ for $\alpha = 16^\circ$, with a red asterisk indicating the maximum peak.

The corresponding amplitude and wavelength are calculated by applying a fast Fourier transform (FFT) to the spanwise velocity w using 601 points across the spanwise direction. A convergence of the FFT result with the considered number of points is shown in Figure 4(a) and a sample FFT result is shown in Figure 4(b) at $tU_\infty/c = 20$ for $\alpha = 16^\circ$. The spanwise wavelength is calculated based on the dominant spatial frequency, which yields the same value throughout the entire linear amplification process. As shown in Figure 5(b), the amplitude grows exponentially in time for $\alpha = 16^\circ$, while it remains constant for $\alpha = 11^\circ$. The dashed vertical lines in Figure 5(b) correspond to the times t_S at which the downstream vortex shedding event begins for each case. Namely, $t_{S_{11^\circ}} U_\infty/c = 10$ and $t_{S_{16^\circ}} U_\infty/c = 6$ correspond to the onset time of the vortex shedding for $\alpha = 11^\circ$ and $\alpha = 16^\circ$, respectively. For $\alpha = 16^\circ$, an exponential growth of about five orders of magnitude is observed and followed by a saturation regime at $tU_\infty/c > 40$. The obtained wavelength of the sinusoidal spanwise velocity is $\lambda_z/c = 0.6$. Note that a similar wavelength of the spanwise instability, in the flow over an NACA0012 airfoil, is obtained elsewhere in the literature. Specifically, [50] reported a wavelength of $\lambda_z/c = 0.66$ for $Re = 1000$ at

$\alpha = 16^\circ$, and [20] reported a spanwise wavelength of $\lambda_z/c = 0.64$ for $Re = 800$ and $\lambda_z/c = 0.62$ for $Re = 1200$ at $\alpha = 20^\circ$. The obtained wavelength can be further compared with those in the cylinder wake by using the corresponding effective Reynolds number [20, 43], $Re_d = Re \sin(\alpha) \simeq 275.6$ for $\alpha = 16^\circ$. As reported in [26], the wavelengths associated with Mode B at $Re = 280$ range from 0.6-1 which aligns closely with $\lambda_z/c = 0.6$ obtained herein.

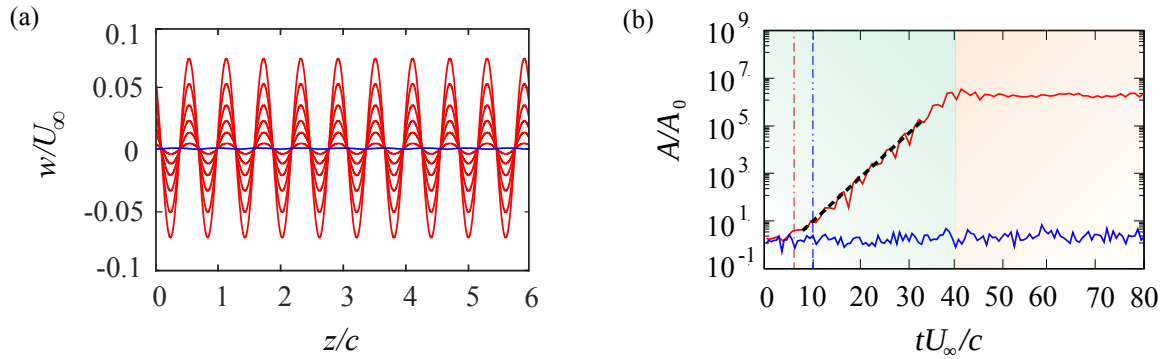


Figure 5. (a) Spanwise velocity w , recorded downstream of the trailing edge at $x/c = 1.5$ and $y = 0$ for the time range $0 < tU_\infty/c < 40$. Blue lines represent $\alpha = 11^\circ$, and red lines represent $\alpha = 16^\circ$. (b) Time evolution of the amplitude of w . The black dashed line corresponds to an exponential fit, $\sim \exp(1.14tU_\infty/c)$. The vertical dash-dotted lines show the onset time of the vortex shedding event, $t_{S_{11^\circ}}U_\infty/c = 10$ (blue line) and $t_{S_{16^\circ}}U_\infty/c = 6$ (red line). The green shaded background area represents the exponential amplification whereas the orange shaded background area identifies the saturation regime and $A_0 = A(t = 0) = 4.75e^{-11}$.

To understand the differences observed above in the wake flow dynamics for the two angles of attack, we next analyze the early-time development of the spanwise instability.

4. Mechanism of the transition to three-dimensionality

As shown in Figure 5(b), the exponential amplification of the spanwise instability, for $\alpha = 16^\circ$, begins approximately at the same time as the vortex shedding event $t_{S_{16^\circ}}U_\infty/c$. Therefore, to understand the origin of the wake three-dimensionality, one must analyze differences in the wake flows at an early-time, prior to $t_{S_{16^\circ}}U_\infty/c$. The instantaneous spanwise vorticity ω_z is displayed by 2D slices at mid-span of the computational domain in Figure 6. While the separation of the laminar boundary layer on the upper side of the airfoil is observed for both angles of attack, the separation point is closer to the leading edge in the case of $\alpha = 16^\circ$, leading to an increased detachment of the boundary layer compared to $\alpha = 11^\circ$ at the same time. For $\alpha = 16^\circ$, this detached boundary layer interacts with the reverse flow from the lower surface (see Figure 6(b2)) and forms a vortex sheet, thus enhancing a Kelvin-Helmholtz-type instability. A strong interaction of a pair of counter-rotating vortices is next observed, see Figure 6(c2) and (d2). The flow at the upper surface is subjected to strong shear effects and then develops a strain field which pulls up small disturbances from the airfoil surface and forms regions of concentrated vortical structures as shown later in Figure 8. Under shearing effects, these streamwise vortices are further subjected to stretching along the extensional strain direction to form downstream vortical structures observed in Figure 3(b). Note that a similar three-dimensional instability mechanism, with the formation of

streamwise vortices, is observed both numerically [51] and experimentally [52], in a plane free shear layer flow. The presence of a strong shear stress and regions of concentrated streamwise vortices at the upper surface of the airfoil, in the case of $\alpha = 16^\circ$, are next analyzed and compared for the two angles of attack.

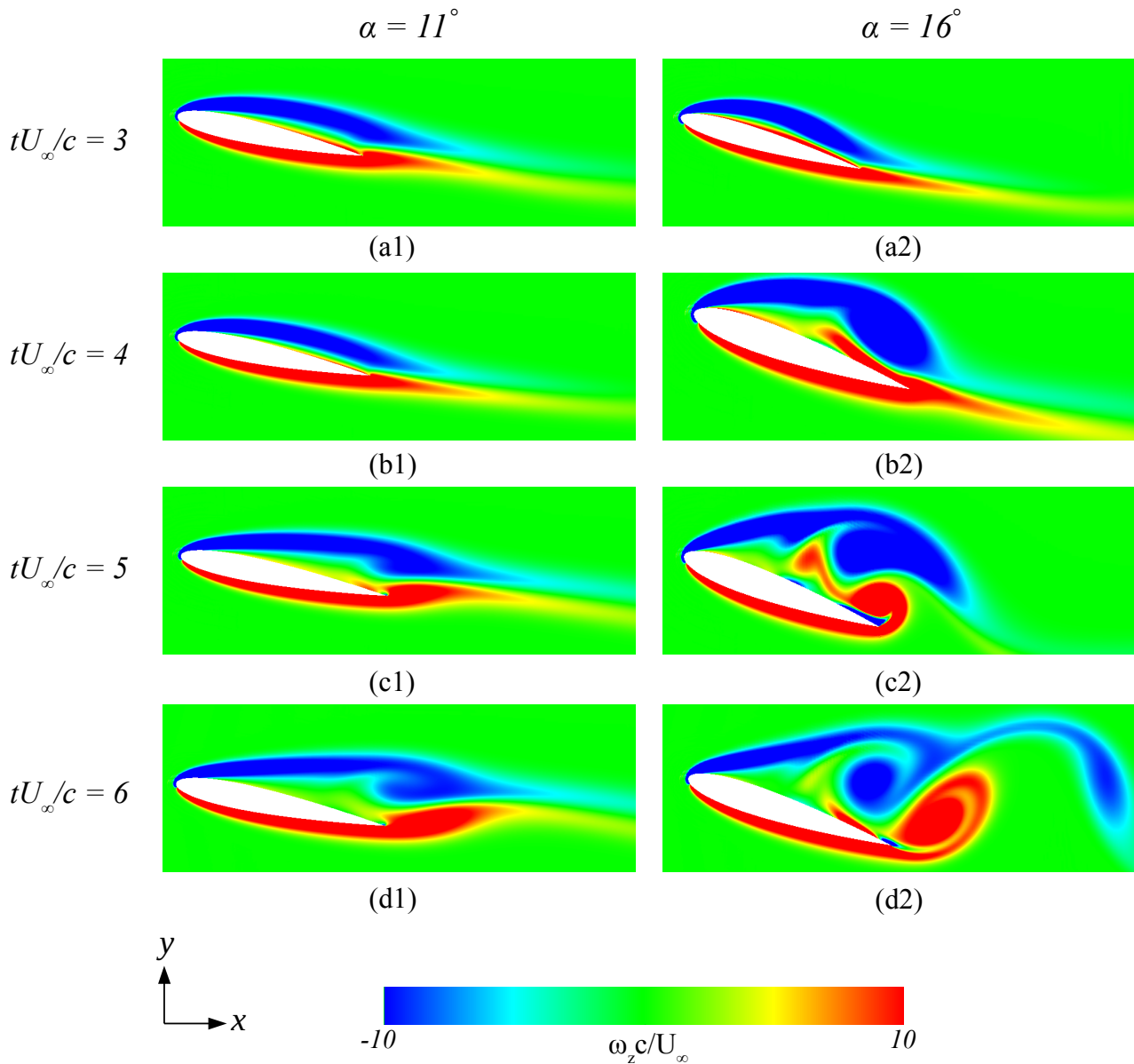


Figure 6. 2D slices showing a time sequence of the spanwise vorticity around the NACA0012 airfoil for the angles of attack $\alpha = 11^\circ$ (a1–d1) and $\alpha = 16^\circ$ (a2–d2).

Figure 7(a) shows the shear stress $\tau_{xy} = \mu \left(\frac{\partial \bar{u}}{\partial y} + \frac{\partial \bar{v}}{\partial x} \right)$, calculated using the time-averaged velocity components (\bar{u}, \bar{v}) along a line in the cross-stream direction, near the trailing edge of the airfoil and passing through the point $(x = 0.8c, z = 0)$ of the x - z plane. The component τ_{yz} of the shear stress in the x - z plane is found to be negligible. \bar{u} and \bar{v} are calculated by averaging instantaneous velocities in time

with $t < t_s$, and shown in Figures 7(b) and (c). A larger cross-stream velocity difference and a reverse flow from the lower surface can be observed at $\alpha = 16^\circ$ compared to $\alpha = 11^\circ$. As shown in Figure 7(a), a greater shear stress is obtained for $\alpha = 16^\circ$ than for $\alpha = 11^\circ$. Therefore, the flow on the upper surface of the airfoil experiences more strain for $\alpha = 16^\circ$ than for $\alpha = 11^\circ$.

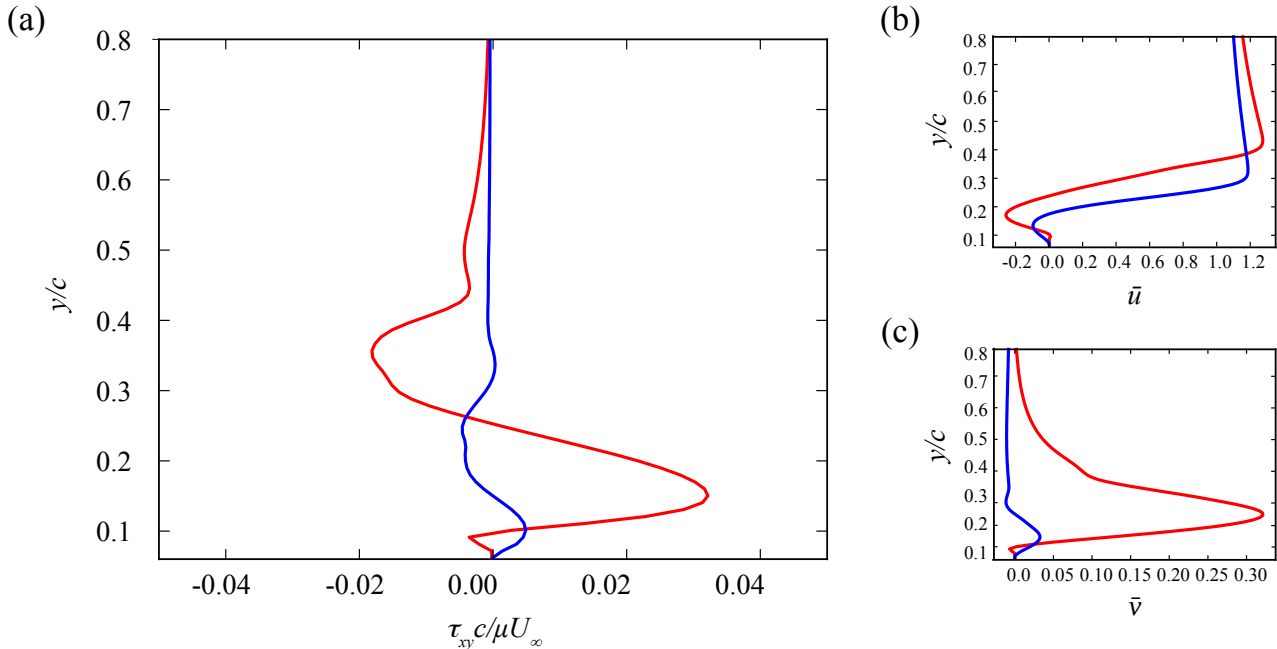


Figure 7. (a) Shear stress τ_{xy} calculated along a vertical line placed at $x/c = 0.8$ and $z = 0$, on the upper surface of the airfoil. The shear stress is calculated using the time averaged velocity components \bar{u} (Figure 7(b)) and \bar{v} (Figure 7(c)), for time smaller than the onset of the vortex shedding event, t_s . The blue color corresponds to $\alpha = 11^\circ$ and the red color corresponds to $\alpha = 16^\circ$.

Next, we use a statistical metric, the normalized squared deviation (also known as the squared z-score) of the velocity to examine similarities and coherent structures present at the upper surface of the airfoil. At each time step, the streamwise velocity fluctuations at each grid point in a z - y plane, $u'(x, y, t)$, are calculated by subtracting the mean velocity.

$$\bar{D}(x, y, t) = \frac{u'(x, y, t)^2}{\sigma_{u'}^2}$$

where $u'(x, y, t)$ represents the velocity fluctuation at each grid point, and $\sigma_{u'}$ is the standard deviation of the velocity fluctuations. This metric measures how far the velocity deviates from its mean value, helping to determine whether a spatial location is typical or unusual compared to the rest of the flow. This is useful for identifying localized structures formed in the flow. Figure 8 shows the normalized squared deviation calculated using streamwise velocities obtained at early times $t < t_s$ (the initial transient flow) for the two different angles of attack, $\alpha = 11^\circ$ and $\alpha = 16^\circ$. While the leading-edge vortex is shed downstream at $\alpha = 11^\circ$, it splits into two on the upper surface of the airfoil, resulting in the appearance of a secondary vortex, similar to what is observed in the instantaneous streamlines of Figure 2(c2). This is attributed to the reverse flow from the lower surface which directly drags the

fluid flow near the lower surface to interact with the trailing-edge vortex, enhancing the strong shear stress observed in Figure 7. A similar mechanism is also shown in the simulations of the flow past a two-dimensional pitching foil [53].

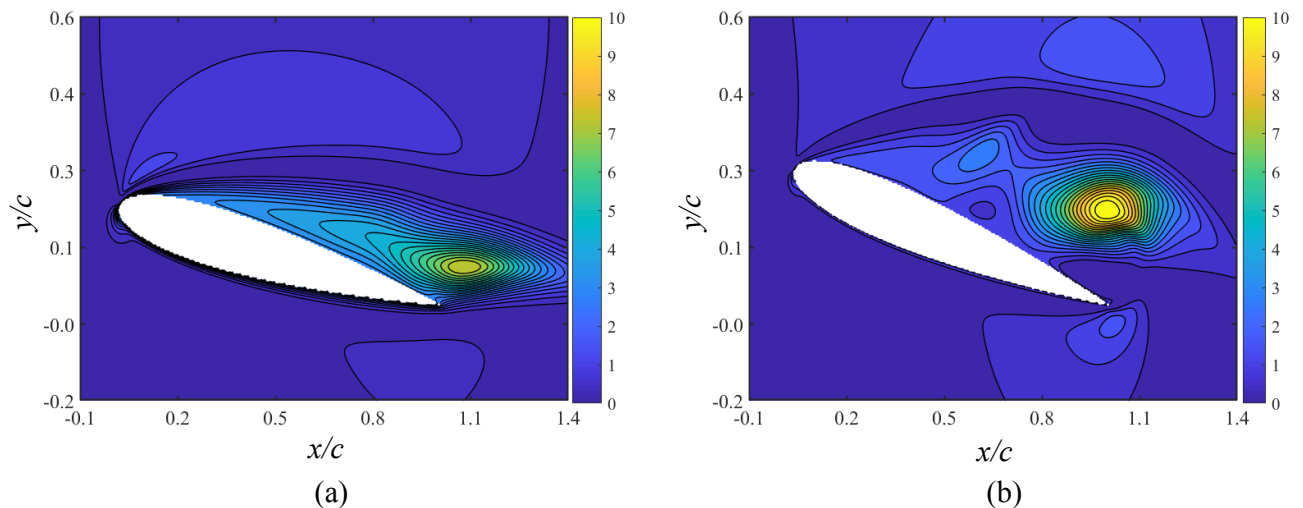


Figure 8. Normalized squared deviation of the streamwise velocity in the x - y plane for times $t < t_S$. (a) $\alpha = 11^\circ$ and (b) $\alpha = 16^\circ$.

The physical mechanisms driving three-dimensional flow behavior at higher angles of attack (AOAs) remain insufficiently understood. The hoped-for outcome of this study is to inform airfoil design by delaying flow separation and managing instabilities such as secondary vortex formation at higher angles of attack, which can improve lift and reduce drag. These findings may also contribute to the development of flow control strategies, such as surface modifications or active control methods, in order to effectively mitigate flow-induced instabilities and enhance performance in critical aerodynamic conditions.

Further work could focus on the experimental validation of the three-dimensional mechanisms discussed above. Additionally, Floquet stability analysis of the three-dimensional unstable modes could offer new insights into three-dimensional wake structures. A higher angle of attack is generally more effective at increasing lift compared to passive boundary layer control. Consequently, a comprehensive understanding of the flow structures that form due to an increased angle of attack is essential for optimizing aerodynamic performance, particularly in enhancing lift and improving stall characteristics during critical flight phases, such as aircraft take-off from the ground, despite a temporary increase in drag. Furthermore, extending the analysis to transonic regimes would aid in assessing the applicability of these findings under high-speed conditions, where flow separation and instabilities become more pronounced.

5. Conclusions

In this work, we performed direct numerical simulations of the flow passing an NACA0012 airfoil using a high-order spectral element method. The three-dimensionality of the wake, induced by the angle of attack, is analyzed at the Reynolds number $Re = 1000$, using two different angles of attack, $\alpha = 11^\circ$

and 16° . First, a boundary layer separation is observed at the upper surface of the airfoil for the two angles of attack with the separation point closer to the leading edge in the case of $\alpha = 16^\circ$. von Kármán vortex shedding is next observed in the two cases. A reverse flow from the lower surface is observed on the top surface of the airfoil for $\alpha = 16^\circ$. In fact, the separated flow from the lower surface of the airfoil turns around to climb onto the upper surface in the case of $\alpha = 16^\circ$. This leads to a strong shear stress on the upper surface and the formation and interaction of counter-rotating vortices.

The three-dimensional flow development in the wake is analyzed through the time evolution of the spanwise component of the velocity w . While a sinusoidal shape with an increasing amplitude is observed for $\alpha = 16^\circ$, w remains approximately zero with no amplification for $\alpha = 11^\circ$. An exponential growth in time of the amplitude is obtained for $\alpha = 16^\circ$ with a wavelength $\lambda_z/c = 0.6$ which agrees very well with reported wavelengths in the literature [50, 20]. The amplification of the sinusoidal w -velocity is shown to start at a similar time to the onset of the vortex shedding event. The early-time analysis of the shear stress on the top surface shows a strong shear stress for $\alpha = 16^\circ$. Thus, the flow on the upper surface experiences a higher strain field which pulls up small disturbances from the airfoil surface and forms regions of concentrated vortical structures. These structures are emphasized by the normalized squared deviation of the streamwise velocity. Under shear effects, the vortical structures are further subjected to stretching and are advected downstream to form the streamwise rib-like vortices observed in the wake of the airfoil for $\alpha = 16^\circ$.

Use of AI tools declaration

The authors declare they have not used Artificial Intelligence (AI) tools in the creation of this article.

Author contributions

Investigation, visualization, writing—original draft preparation, H.K.; conceptualization, methodology, supervision, writing—review and editing, G.G.A. All authors have read and agreed to the published version of the manuscript.

Conflict of interest

The authors declare no conflicts of interest.

References

1. Romeo G, Frulla G, Cestino E, et al. (2004) HELIPLAT: Design, aerodynamic, structural analysis of long-endurance solar-powered stratospheric platform. *J Aircraft* 41: 1505–1520. <https://doi.org/10.2514/1.2723>
2. Hassanalian M, Abdelkefi A (2017) Classifications, applications, and design challenges of drones: A review. *Prog Aerosp Sci* 91: 99–131. <https://doi.org/10.1016/j.paerosci.2017.04.003>
3. Carmichael BH (1981) Low-Reynolds number airfoil survey. 165803, NASA.
4. Lin YF, Lam K, Zou L, et al. (2013) Numerical study of flows past airfoils with wavy surfaces. *J Fluid Struct* 36: 136–148. <https://doi.org/10.1016/j.jfluidstructs.2012.09.008>

5. Zhang W, Cheng W, Gao W, et al. (2015) Geometrical effects on the airfoil flow separation and transition. *Comput Fluids* 116: 60–73. <https://doi.org/10.1016/j.compfluid.2015.04.014>
6. Karasu I, Genç MS, Açıkel HH (2013) Numerical study on low Reynolds number flows over an Aerofoil. *J Appl Mech Eng* 2: 1000131.
7. Amiralaei MR, Alighanbari H, Hashemi SM (2010) An investigation into the effects of unsteady parameters on the aerodynamics of a low Reynolds number pitching airfoil. *J Fluids Struct* 26: 979–993. <https://doi.org/10.1016/j.jfluidstructs.2010.06.004>
8. Mueller TJ (1999) Aerodynamic Measurements at Low Reynolds Numbers for Fixed Wing Micro-Air Vehicles, in: RTO AVT/VKI Special Course on Development and Operation of UAVs for Military and Civil Applications, Hessert Center for Aerospace Research, University of Notre Dame, VKI, Belgium, 13–17.
9. Munday PM, Taira K, Suwa T, et al. (2015) Nonlinear Lift on a Triangular Airfoil in Low-Reynolds-Number Compressible Flow. *J Aircraft* 52: 924–931. <https://doi.org/10.2514/1.C032983>
10. Kurtulus DF (2016) On the wake pattern of symmetric airfoils for different incidence angles at $Re = 1000$. *Int J Micro Air Veh* 8: 109–139. <https://doi.org/10.1177/1756829316653700>
11. Rossi E, Colagrossi A, Oger G, et al. (2018) Multiple bifurcations of the flow over stalled airfoils when changing the Reynolds number. *J Fluid Mech* 846: 356–391. <https://doi.org/10.1017/jfm.2018.189>
12. Genç MS, Karasu İ, Açıkel HH (2012) An experimental study on aerodynamics of NACA2415 aerofoil at low Re numbers. *Exp Therm Fluid Sci* 39: 252–264. <https://doi.org/10.1016/j.expthermflusci.2012.01.029>
13. Ducoin A, Loiseau JC, Robinet JC (2016) Numerical investigation of the interaction between laminar to turbulent transition and the wake of an airfoil. *Eur J Mech B-Fluid* 57: 231–248. <https://doi.org/10.1016/j.euromechflu.2016.01.005>
14. Shelton A, Abras J, Hathaway B, et al. (2005) An investigation of the numerical prediction of static and dynamic stall. in: *Proceedings of the 61st American Helicopter Society Annual Forum*, 61: 1826.
15. Genç MS (2010) Numerical Simulation of Flow over a Thin Aerofoil at a High Reynolds Number Using a Transition Model. *P I Mech Eng C-J Mec* 224: 2155–2164. <https://doi.org/10.1243/09544062JMES2121>
16. Hain R, Kähler C J, Radespiel R (2019) Dynamics of laminar separation bubbles at low-Reynolds-number aerofoils. *J Fluid Mech* 630: 129–153. <https://doi.org/10.1017/S0022112009006661>
17. Jones LE, Sandberg RD, Sandham ND (2008) Direct numerical simulations of forced and unforced separation bubbles on an airfoil at incidence. *J Fluid Mech* 602: 175–207. <https://doi.org/10.1017/S0022112008000864>
18. Zhou Y, Alam MM, Yang HX, et al. (2011) Fluid forces on a very low Reynolds number airfoil and their prediction. *Int J Numer Method H* 32: 329–339. <https://doi.org/10.1016/j.ijheatfluidflow.2010.07.008>
19. Wang S, Zhou Y, Alam MM, et al. (2014) Turbulent intensity and Reynolds number effects on an airfoil at low Reynolds numbers. *Phys Fluids* 26: 115107. <https://doi.org/10.1063/1.4901969>

20. Hoarau Y, Braza M, Ventikos Y, et al. (2003) Organized modes and the three-dimensional transition to turbulence in the incompressible flow around a NACA0012 wing. *J Fluid Mech* 496: 63–72. <https://doi.org/10.1017/S0022112003006530>
21. Huang RF, Wu JY, Jeng JH, et al. (2001) Surface flow and vortex shedding of an impulsively started wing. *J Fluid Mech* 441: 265–292. <https://doi.org/10.1017/S002211200100489X>
22. Lissaman PBS (1983) Low-Reynolds-Number Airfoils. *Annu Rev Fluid Mech* 15: 223–239.
23. Klose BF, Spedding GR, Jacobs GB (2021) Direct numerical simulation of cambered airfoil aerodynamics at $Re = 20,000$. *arXiv*. <https://doi.org/10.48550/arXiv.2108.04910>
24. Williamson CHK (1988) The existence of two stages in the transition to three-dimensionality of a cylinder wake. *Phys Fluids* 31: 3165–3168.
25. Williamson CHK (1996) Vortex dynamics in the cylinder wake. *Ann Rev Fluid Mech* 28: 477–539.
26. Barkley D, Henderson RD (1996) Three-dimensional Floquet stability analysis of the wake of a circular cylinder. *J Fluid Mech* 322: 215–241. <https://doi.org/10.1017/S0022112096002777>
27. Robichaux J, Balachandar S, Vanka SP (1999) Three-dimensional Floquet instability of the wake of square cylinder. *Phys Fluids* 11: 560–578. <https://doi.org/10.1063/1.869930>
28. Saha AK, Biswas G, Muralidhar K (2003) Three-dimensional study of flow past a square cylinder at low Reynolds numbers. *Int J Heat Fluid Flow* 24: 54–66. [https://doi.org/10.1016/S0142-727X\(02\)00208-4](https://doi.org/10.1016/S0142-727X(02)00208-4)
29. Luo SC, Tong XH, Khoo BC (2007) Transition phenomena in the wake of a square cylinder. *J Fluids Struct* 23: 227–248. <https://doi.org/10.1016/j.jfluidstructs.2006.08.012>
30. Luo SC, Chew YT, Ng YT (2003) Characteristics of square cylinder wake transition flows. *Phys Fluids* 15: 2549–2559. <https://doi.org/10.1063/1.1596413>
31. Barkley D, Tuckerman LS, Golubitsky M (2000) Bifurcation theory for three-dimensional flow in the wake of a circular cylinder *Phys Rev E* 61: 5247–5252. <https://doi.org/10.1103/PhysRevE.61.5247>
32. Blackburn HM, Lopez JM (2003) On three-dimensional quasiperiodic Floquet instabilities of two-dimensional bluff body wakes. *Phys Fluids* 15: L57–L60. <https://doi.org/10.1063/1.1591771>
33. Meneghini JR, Carmo BS, Tsiloufas SP, et al. (2011) Wake instability issues: From circular cylinders to stalled airfoils. *J Fluids Struct* 27: 694–701. <https://doi.org/10.1016/j.jfluidstructs.2011.03.018>
34. Deng J, Sun L, Shao X (2017) Floquet stability analysis in the wake of a NACA0015 airfoil at post-stall angles of attack. *Phys Fluids* 29: 094104. <https://doi.org/10.1063/1.5003578>
35. He W, Gioria RS, Pérez JM, et al. (2017) Linear instability of low Reynolds number massively separated flow around three NACA airfoils. *J Fluid Mech* 811: 701–741. <https://doi.org/10.1017/jfm.2016.778>
36. Gupta S, Zhao J, Sharma A, et al. (2023) Two- and three-dimensional wake transitions of a NACA0012 airfoil. *J Fluid Mech* 954: A26. <https://doi.org/10.1017/jfm.2022.958>
37. Kouser T, Xiong Y, Yang D, et al. (2021) Direct numerical simulations on the three-dimensional wake transition of flows over NACA0012 airfoil at $Re=1000$. *Int J Micro Air Veh* 13: 1–15. <https://doi.org/10.1177/17568293211055656>

38. Xia T, Dong H, Yang L, et al. (2021) Investigation on flow structure and aerodynamic characteristics over an airfoil at low Reynolds number—A review. *AIP Adv* 11: 050701. <https://doi.org/10.1063/5.0044717>
39. Patera AT (1984) A spectral element method for fluid dynamics: Laminar flow in a channel expansion. *J Comput Phys* 54: 468–488.
40. Fischer P, Kruse J, Mullen J, et al. Nek5000: Open source spectral element CFD solver. *Argonne National Laboratory, Mathematics and Computer Science Division*, Argonne, IL, Available from: <https://nek5000.mcs.anl.gov/index.php/MainPage2>.
41. Deville MO, Fischer PF, Mund EH (2002) *High-Order Methods for Incompressible Fluid Flow*, Cambridge Monographs on Applied and Computational Mathematics. Cambridge University Press.
42. Cummings RM, Morton SA, Mason WH (2015) *Applied Computational Aerodynamics*, Cambridge Aerospace Series, Cambridge University Press.
43. Hoarau Y, Braza M, Ventikos Y, et al. (2006) First stages of the transition to turbulence and control in the incompressible detached flow around a NACA0012 wing. *Int J Heat Fluid Fl* 27: 878–886. <https://doi.org/10.1016/j.ijheatfluidflow.2006.03.026>
44. Uranga A, Persson PO, Drela M, et al. (2011) Implicit Large Eddy Simulation of transition to turbulence at low Reynolds numbers using a discontinuous galerkin method. *Int J Numer Meth Eng* 87: 232–261. <https://doi.org/10.1002/nme.3036>
45. Khalid MSU, Akhtar I (2012) Characteristics of Flow Past a Symmetric Airfoil at Low Reynolds Number: A Nonlinear Perspective. *ASME International Mechanical Engineering Congress and Exposition*, American Society of Mechanical Engineers, 167–175. <https://doi.org/10.1115/IMECE2012-87389>
46. Hongquan Z (1998) Centrifugal instability and the rib vortices in the cylinder wake. *Acta Mech Sinica* 14: 104–112. <https://doi.org/10.1007/BF02487745>
47. Agbaglah G, Mavriplis C (2017) Computational analysis of physical mechanisms at the onset of three-dimensionality in the wake of a square cylinder. *J Fluid Mech* 833: 631–647. <https://doi.org/10.1017/jfm.2017.713>
48. Agbaglah G, Mavriplis C (2019) Three-dimensional wakes behind cylinders of square and circular cross-section: early and long-time dynamics. *J Fluid Mech* 870: 419–432. <https://doi.org/10.1017/jfm.2019.265>
49. Kokash H, Agbaglah GG (2022) On the origin of mode B instability of the wake of a square cylinder. *Phys Fluids* 34: 074116. <https://doi.org/10.1063/5.0101403>
50. Kouser T, Xiong Y, Yang D, et al. (2022) Numerical study on drag reduction and wake modification for the flows over a hydrofoil in presence of surface heterogeneity. *Adv Mech Eng* 14: 1–14. <https://doi.org/10.1177/168781402210753>
51. Lasheras JC, Choi H (1988) Three-dimensional instability of a plane free shear layer: an experimental study of the formation and evolution of streamwise vortices. *J Fluid Mech* 189: 53–86. <https://doi.org/10.1017/S0022112088000916>
52. Pierrehumbert RT, Widnall SE (1982) The two- and three-dimensional instabilities of a spatially periodic shear layer. *J Fluid Mech* 114: 59–59. <https://doi.org/10.1017/S0022112082000044>

-
53. Tseng CC, Hu HA (2015) Flow dynamics of a pitching foil by eulerian and lagrangian viewpoints. *AIAA J* 54: 2. <https://doi.org/10.2514/1.J053619>



AIMS Press

©2024 the Author(s), licensee AIMS Press. This is an open access article distributed under the terms of the Creative Commons Attribution License (<https://creativecommons.org/licenses/by/4.0>)